Simulating the growth of amorphous organic thin films

Carl Degitz, Manuel Konrad, Simon Kaiser, Wolfgang Wenzel *

Institute of Nanotechnology, KIT Campus North, Hermann-von-Helmholtz-Platz 1, 76344, Eggenstein-Leopoldshafen, Germany

ARTICLE INFO

Keywords:
Molecular dynamics
Monte Carlo
OLED
Simulation

ABSTRACT

Physical vapor deposition is used widely to produce organic electronics devices, in particular for OLEDs in smartphones, TVs and other display applications. Despite its long history, recent years have seen a number of surprising observations, such as deposition-induced emitter orientation and built-in electrostatic potentials in thin organic films. Modeling the details of these effects is complicated by the long time scales involved in the underlying processes. In this paper, we compare two different modeling approaches, which both aim to simulate the physical vapor deposition (PVD) process for small organic molecules. We compare a molecular dynamics approach, based on a classical bead-spring force field and time integration, with a Metropolis Monte Carlo approach, where the intramolecular degrees are limited to the torsional rotations. To analyze the resulting structures, we calculate the density and radial distribution functions (RDF) of all films. We observe a good agreement for the RDFs, but an approximately 10% higher density for the films generated by the molecular dynamics approach. Additionally, we investigate the anisotropic nature of such morphologies by calculating the ordinary and extra-ordinary refractive index for each material. Finally, we calculate electron and hole mobilities with an Kinetic Monte Carlo protocol.

1. Introduction

Since discovery of the first organic light emitting diode (OLED) in 1987 [1], OLED technology has made its way into everyday life through smartphones, TVs, and wearable devices. In an OLED display, all pixels can be turned on or off independently of each other, which enables a theoretically perfect contrast ratio. Due to this self-emitting nature, OLED displays can be built much thinner than a conventional LCD display which usually consists of a backlight with several polarization and filter layers on top. The mechanical flexibility achieved through this thin design also enables foldable or rollable displays which already entered the consumer market. In contrast to the initial two-layer device demonstrated by Tang et al. modern OLED stacks consist of many different layers which, for example, in the case of an emissive layer, are often a mixture of two to three different organic materials [2]. The extreme thin film thickness, in the order of 10–100 nm of OLED displays is achieved by physical vapor deposition (PVD) or solution processing techniques, usually resulting in an amorphous thin film of the organic material. Crucial device properties like charge carrier mobility or photon outcoupling efficiency are directly related to the disorder and orientation of molecules in the amorphous film.

Recently, many interesting effects have been observed that directly relate to the thin film deposition process. Thin organic films generated by PVD show a horizontal molecular orientation with respect to the deposition direction, which manifests itself in an anisotropic refractive index [3,4]. The degree of orientation anisotropy is linked to the deposition process and can be tuned by manipulating the substrate temperature [5,6,7]. Besides this thermal manipulation, adjusting the deposition rate in specific patterns also influences the molecular orientation which directly affects device parameters like light emission efficiency, chromaticity coordinate, and turn on voltage [8].

Many of these observations are difficult to explain on the basis of experimental data alone, because in-situ and/or in-operando observation of the film is difficult. Development of realistic modeling techniques to describe the growth of an organic thin film morphology can help ameliorate this situation. Such techniques could also be helpful in device modeling [9,10]. Here we present two different modeling approaches which aim to simulate the physical vapor deposition of small organic molecules. In the first approach, we use a Monte-Carlo protocol [11] where each molecule is frozen after deposition, which results in a near perfect linear scaling of the calculation time with respect to the system size. In the second approach, we use molecular dynamics simulations,

---

* Corresponding author.
E-mail addresses: carl.degitz@partner.kit.edu (C. Degitz), manuel.konrad@kit.edu (M. Konrad), simon.kaiser@kit.edu (S. Kaiser), wolfgang.wenzel@kit.edu (W. Wenzel).

where all atoms move in every time step. The latter approach permits – in principle – the treatment of collective effects during the deposition process at the cost of higher computational effort.

To evaluate both methods, we generate structures for four small organic molecules (see Fig. 1): 2,9-Dimethyl-4,7-diphenyl-1,10-phenanthroline (BCP) and 4,7-Diphenyl-1,10-phenanthroline (BPhen), which are commonly used in the electron transport or hole blocking layer of an OLED as well as N,N′-Di(1naphthyl)-N,N′-diphenyl-(1,1′-biphenyl)-4,4′-diamine (NPB) and 4,4′-Bis(N-carbazolyl)1,1′-biphenyl (CBP), which serve as hole transport and host material respectively. After the deposition simulation we compare the simulated densities to previously measured values from Xiang et al. [12] We also calculate the radial distribution functions and the ordinary and extra-ordinary refractive indices. Finally, we evaluate how the generated structures affect the field dependent electron and hole mobility using an *ab-initio* multiscale model [13,14,15,16].

2. Deposition simulation

2.1. Monte Carlo approach

To model the PVD process we use an improved version of the DEPOSIT deposition protocol published by Neumann et al., in 2013 [11]. In this protocol, the deposition is performed for one molecule at a time, enabling a linear scaling of the computation time with respect to system size. However, since collective effects are completely neglected, e.g., crystallization, this method is only applicable to amorphous organic semiconductors and its restrictions may even impact the film morphology there. The total energy of the deposited molecule consists of an intermolecular and intramolecular contribution. The intermolecular part comprises the Van-der-Waals attraction and Pauli repulsion represented by a Lennard-Jones term E_{LJ}, as well as the electrostatic interaction between partial charges represented by a Coulomb term E_{ES}. In the DEPOSIT approach, changes of bond lengths and bond angles are neglected, because they change little for stiff organic molecules, only torsional rotations around dihedral angles, represented by E_{DH}, are considered:

$$E_{\mathrm{tot}} = E_{\mathrm{LJ}} + E_{\mathrm{ES}} + E_{\mathrm{DH}} \tag{1}$$

To reduce the computational effort, a grid wise interpolation is used to calculate the intermolecular contributions in every MC step. The electrostatic grid is simply the electrostatic potential created by all previously deposited molecules. The Lennard-Jones contribution consists of a separate grid for every Lennard-Jones parameter combination existing in the current simulation. To parameterize these interactions, we chose the partial charges and Lennard-Jones parameters from the GROMOS 54A7 force field [17,18,19], since this was the force field used in the MD simulations later on. The forcefields for the internal torsional rotations are extracted from the relevant dihedral terms of the GROMOS forcefield.

The deposition cycle for a single molecule is illustrated in Fig. 2 (a). The deposition is split into several independent simulated annealing (SA) cycles, which run in parallel. During each SA-cycle, a previously specified number of Monte Carlo (MC) steps is performed. In each MC step, a random move (translation, rotation or rotation of dihedral angles) is performed and the total energy evaluated. Every move is either accepted or rejected based on the Metropolis-Monte-Carlo criterion [20]. During the SA-Cycle, the simulation temperature starts at a high value $T_{\mathrm{high}} = 4000\mathrm{K}$ for the first step and gets gradually adjusted to the final value $T_{\mathrm{low}} = 300\mathrm{K}$:

$$T_n = T_{high} \cdot \left(\frac{T_{low}}{T_{high}}\right)^{\frac{n}{N}} \tag{2}$$

Where n is the current step and N is the total number of MC steps per deposition cycle. After every SA-cycle has finished, the deposited molecule is chosen by looping through the final energies and accepting them based on the Metropolis criterium at temperature T_{low}. After deposition of one molecule, the electrostatic and Lennard Jones grids are updated by adding the contributions of the molecule to the previous grid and the next deposition cycle starts.

2.2. Molecular dynamics approach

In the Molecular Dynamics (MD) approach, we tried to replicate the MC deposition protocol as best as possible, while also including collective movements and more flexible molecules. We use a deposition scheme similar to the one used by Dalal et al. [5]. In their approach they used a coarse-grained model of 6 Lennard-Jones spheres to represent the

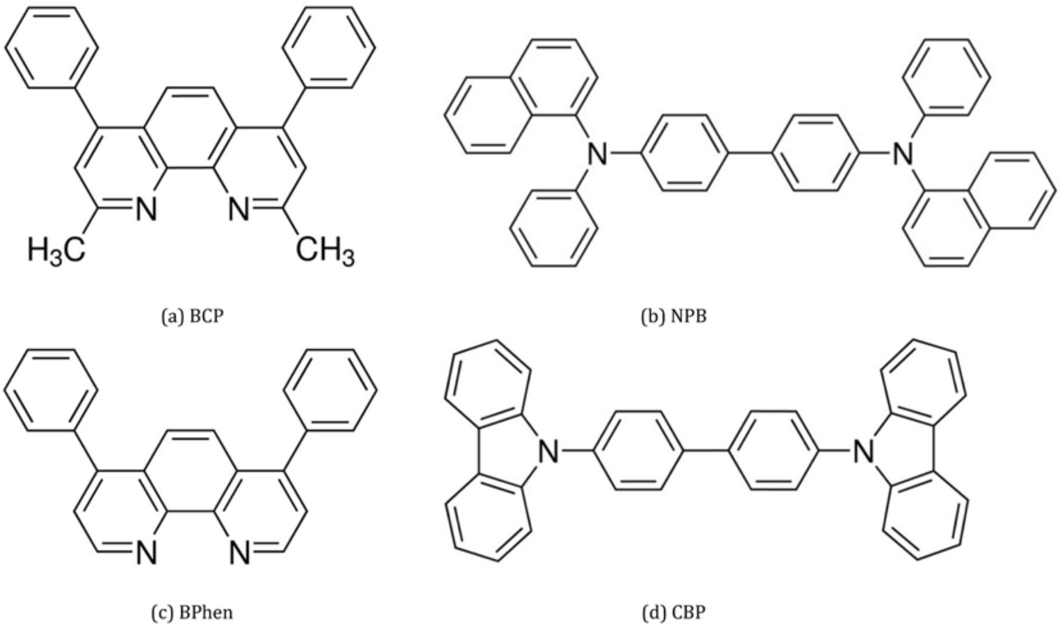

(a) BCP (b) NPB

(c) BPhen (d) CBP

Fig. 1. Chemical structures of 2,9-Dimethyl-4,7-diphenyl-1,10-phenanthroline (BCP), N,N′-Di(1-naphthyl)-N,N′-diphenyl-(1,1′-biphenyl)-4,4′-diamine (NPB), 4,7-Diphenyl-1,10phenanthroline (BPhen) and 4,4′-Bis(N-carbazolyl)-1,1′-biphenyl (CBP).

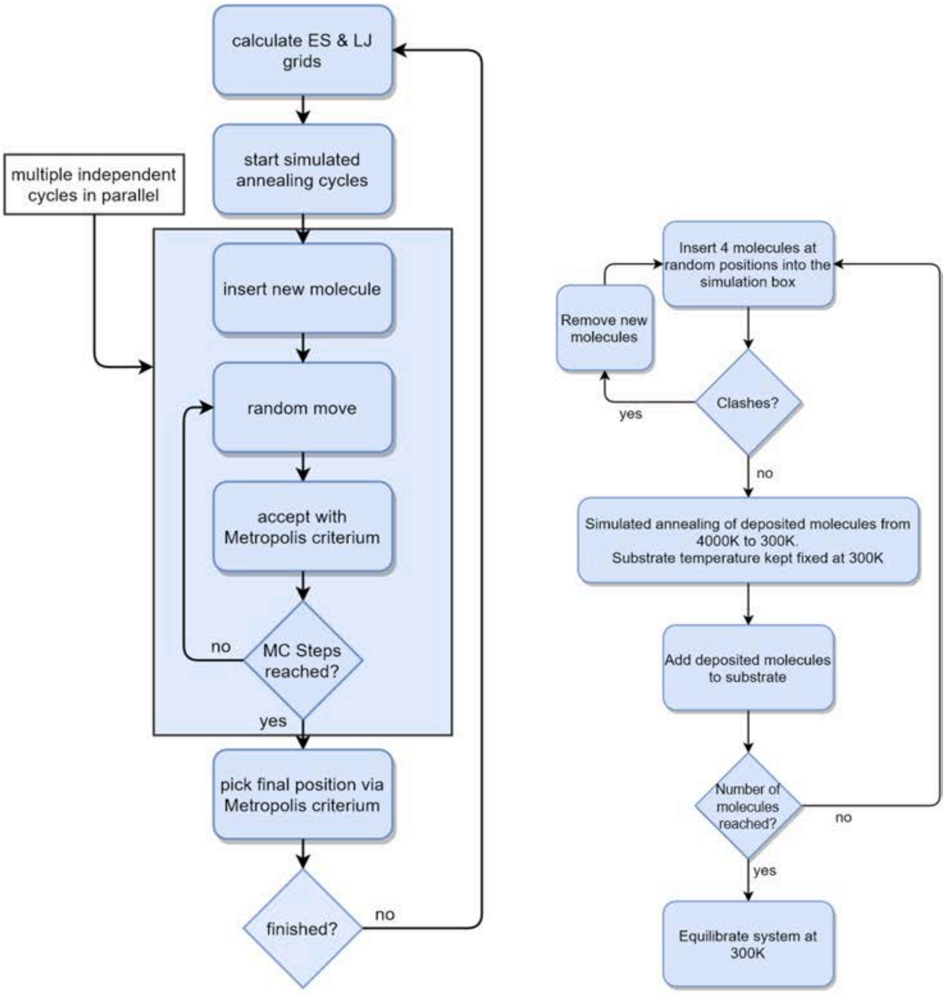

(a) MC (b) MD

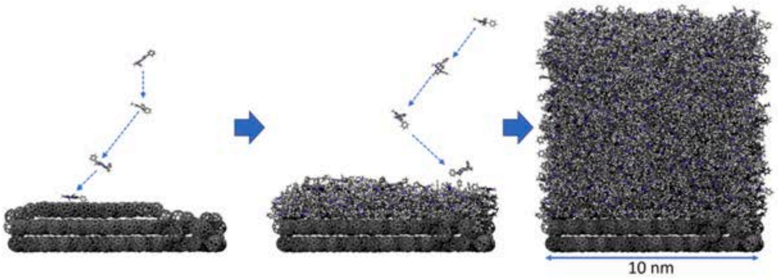

(c) PVD simulation

Fig. 2. Workflow Diagrams for the Monte Carlo approach (a) and the Molecular Dynamics approach (b). Snapshots from the deposition simulation (c): The simulation starts with a C60 substrate onto which molecules are being deposited. In the MD case previously deposited molecules can move during the whole simulation, in the MC case molecules are frozen in place after deposition.

organic hole transport material TPD (N,N′-Bis-(3-methylphenyl)-N, N'diphenylbenzidin). Combined with their deposition scheme, they were able to reproduce the thermal dependency of molecular orientation during the PVD process. In contrast to this we use the all atom GROMOS [17,18,19] force field to describe the molecular interactions in our study, but keep the general deposition scheme, which is illustrated in Fig. 2 (b). Newly inserted molecules are initialized with a velocity of 0.005 $\text{Å}\text{fs}^{-1}$ towards the substrate surface. Similar studies have been performed by Zannoni et al. where they simulated film growth of the well-known organic semiconductor Pentacene [21,22].

We use a simulation box with two-dimensional periodic boundary conditions in the film plane and harmonic wall potentials in the third dimension to prevent atoms from leaving the simulation. After the deposition, we equilibrated the final structure at 300 K for 20 ps followed by a cooling down to 0.1 K for 400 ps, during which the center of mass of every molecule was kept fixed, ensuring that the density and packing does not change as a result of the cooling process. This reduces fluctuations of bond lengths and bond angles in the final snapshot, which is necessary since the subsequent DFT calculations on our structure would be heavily influenced from out of equilibrium bonds. This also makes the final structures more comparable to the MC approach, where bond lengths and bond angles are fixed by default. To preserve the packing of our molecules and the density of our film, we keep the center of mass of each molecule fixed during the cooling process. All MD simulations were performed with the LAMMPS package, which is available on http://lammps.sandia.gov [23].

2.3. Simulation parameters

To quantitatively analyze both simulation methods, we create 10 independent thin films of the following materials: BCP, BPhen, NPB and CBP. In both methods, our systems obey 2D-periodic boundary conditions in x and y direction with a box size of 10 by 10 nm. The box was limited to 20 nm in z-direction in both approaches. For the long-range electrostatic interactions in the MD simulation, the particle-particle particle-mesh method (PPPM) is used, which is implemented in LAMMPS. It requires 3D periodic boundary conditions; therefore the implementation adds an implicit vacuum slab in z-direction to reduce the interaction with images in this dimension. In our case, an additional 20 nm of vacuum have been added. To obtain equal initial conditions, we prepare a thin film of approximately two monolayers of C_{60}, which serves as substrate for each sample. For the MC deposition, we use 200000 steps and 30 simulated annealing cycles per molecule, with $T_{\text{high}} = 4000\text{K}$ and $T_{\text{low}} = 300\text{K}$. The higher temperature is chosen to enable the currently deposited molecule to overcome energy barriers more easily during the beginning of the deposition. In the MD approach, we use 2000 steps of initial equilibration followed by 10000 steps of simulated annealing per deposition cycle. We keep all bonds involving hydrogen atoms fixed during the simulation, thus enabling a timestep Δt of 2 fs. In both methods, the number of deposited molecules is chosen in a way that we fill a $10 \times 10 \times 10\ \text{nm}^3$ box with a density of approximately 1 g/cm^3. All MD input files were generated with the Automated Topology Builder [24].

3. Results

3.1. Density

The density was calculated for slices of increasing thickness h around the center of the morphology. The calculated density quickly converges to a constant regime with increasing values of h and falls of when the slice reaches the edges of the simulation box in z direction. The final density is defined as the average density in the constant regime. The so calculated densities are shown in Fig. 3. The results for the MD part are overall in better agreement with the experimental values. The density of the MC films is underestimated for all materials with respect to the experimental results as well as the MD results. In general, the total density of a film depends on (a) the local packing of molecules mostly given by the molecular size and flexibility and (b) long range packing achieved by collective movements during the deposition. The underestimation of the MC densities can be linked to both contributions: (a) The rigidity of the dihedral fragments effectively limits the local packing compared to MD, where two molecules can bend “around” each other more freely (see Fig. 4). (b) Due to the frozen substrate approximation, collective movements are completely prohibited.

3.2. Radial distribution function

To further analyze the local packing we calculate the radial distribution function (RDF) $g(\vec{r})$ for all materials: For every simulated morphology we choose molecules from a slab of height 2 nm around the center of the morphology. For each molecule in the slab, we calculate the center of mass distances to all other molecules inside a 2.5 nm cutoff. With this we ensure that no edge effects, due to the vacuum and substrate boundaries in z-direction, influence the result. The RDF is then calculated with the histogram entry $H(r)$ at distance r, the number of samples N, the volume of each distance bin $V(r)$ and the number density of the film ρ_0:

$$g(r) = \frac{H(r)}{N \cdot V(r) \cdot \rho_0} \tag{3}$$

The final RDF shown in Fig. 5 is obtained by taking the average of all 10 structures per molecule and method. For all molecules, we observe a constant value of 1 for distances greater than approximately 15 Å, which confirms the amorphous nature of the generated films. For CBP and NPB the minimum distance is about 1 Å smaller in MD than in MC, in contrast to BCP and BPhen where no difference is observed. This can be

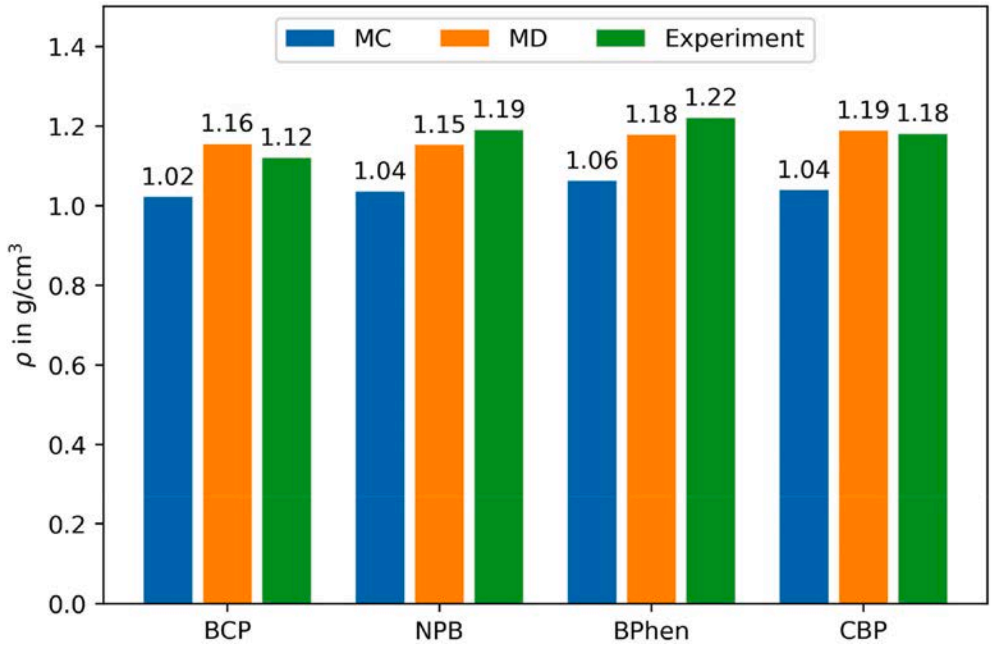

Fig. 3. Densities of BCP, NPB, BPhen and CBP. In green are the measured values by Xiang et al. [12], in orange the values from the MD approach and in blue the values obtained by the MC protocol. Each simulated value is a mean value of 10 independent simulations, the standard deviation was below 0.003 g/cm^3. The experimental uncertainty is 0.01 g/cm^3. (For interpretation of the references to colour in this figure legend, the reader is referred to the Web version of this article.)

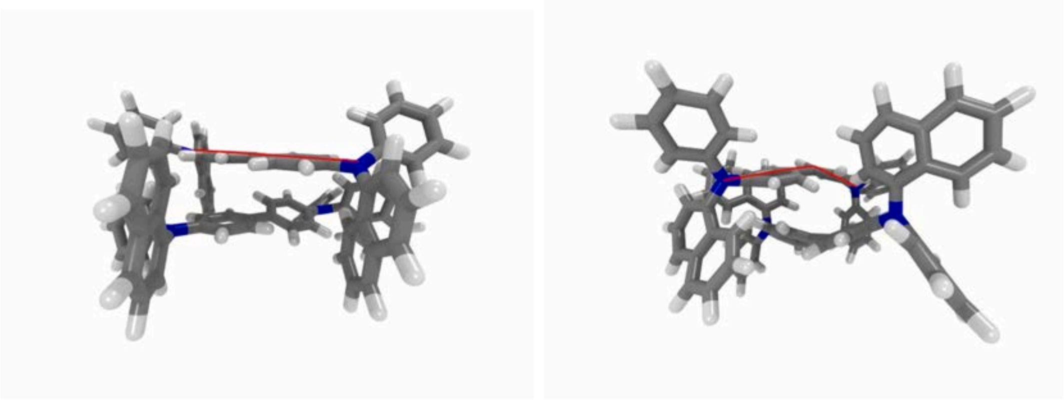

(a) MC approach (b) MD approach

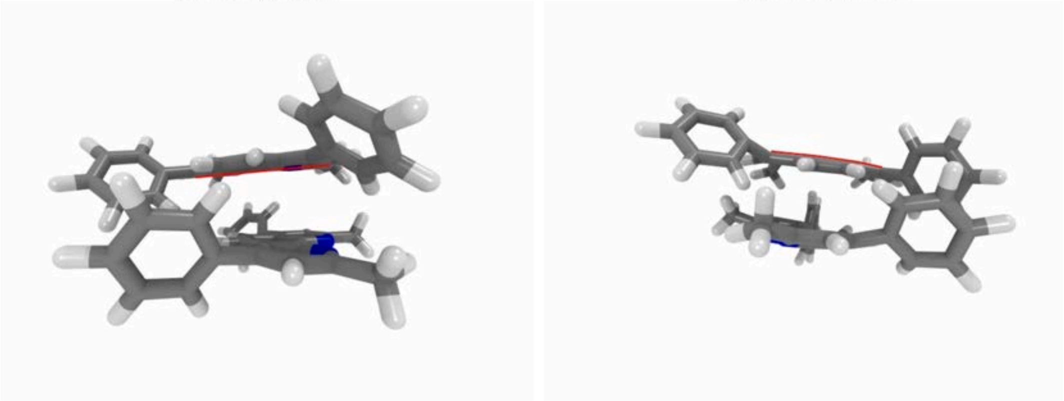

(c) MC approach (d) MD approach

Fig. 4. Minimal center of mass distance snapshots for NPB (a) and (b) as well as BCP (c) and (d). The bending of the molecular axis through the biphenyl core of NPB and phenanthroline core of BCP is highlighted in red. The flexible core of NPB enables a better local packing in the MD approach vs. the MC approach, while for BCP no difference is observed. The same behavior can be observed for CBP and BPhen, pictures of this can be found in the SI. (For interpretation of the references to colour in this figure legend, the reader is referred to the Web version of this article.)

attributed to the fact that the rigid fragment approximation is a better fit for the stiff phenanthroline core of BCP and BPhen than for the biphenyl core of NPB and CBP (see Fig. 4). Comparing the overall shape of the RDF, we observe a peak at 5 Å for the MC structures of BCP and BPhen, which is much less prominent in the MD morphology of BCP. This peak could be an indicator that there is a higher ordering in the MC structure of BCP compared to the MD structure, which is further investigated in the following sections.

3.3. *Orientation of dihedral fragments*

To further analyze the ordering in our simulated morphologies, we look at the orientation of the dihedral fragments with respect to the growth direction (z-axis). For this we define a fragment plane as the plane with minimal distance to all atoms in the specific fragment. We chose $\cos^2\theta_z$ as and order parameter where θ_z is the angle between the plane normal and the z-axis. The orientation histograms of the phenanthrolin core of BCP and the core phenyl rings of NPB are depicted in Fig. 6, the histograms for the other dihedral fragments and materials can be found in the SI.

We observe a clear difference between MC and MD structures when looking at the orientation of these core fragments. The MD protocol shows a nearly isotropic orientation of the dihedral fragments for all materials, with a slightly anisotropic orientation of the core fragments towards lying flat on the surface, which is strongest for CBP. In the MC case the anisotropy of the core fragments is much larger for CBP, BPhen and BCP. For NPB both methods differ only slightly, but also towards favoring a flatter orientation in case of the MC structures. For the outer fragments the ordering is close to isotropic and both methods differ only slightly. These results a suggest that especially the BPhen and BCP films are packed qualitatively different in both methods.

3.4. *Refractive indices*

Besides their amorphous nature, thin films generated by PVD often show anisotropic behavior in the growth direction z compared to isotropic behavior in the x-y-plane. This can manifest itself in measurable quantities like the giant surface potential [26,27], orientation of emitter molecules [28,29] or birefringence [4,3,30]. These effects are all linked to a preferred geometric orientation of the molecular structure. To further quantify this different ordering in our films, we calculate the ordinary and extra-ordinary refractive indices for our simulated structures and compare them to values obtained by ellipsometry measurements [25]. In these measurements only CBP shows birefringence.

To calculate the refractive index *n* we use the well-known *Clausius-Mossotti* equation,

$$\frac{\varepsilon \quad 1}{\varepsilon \quad 2} \quad \frac{N\alpha}{3\varepsilon_0} \tag{4}$$

which connects the macroscopic relative permittivity to the microscopic molecular polarization α and the number density N of the molecules. Technically this equation is only valid in the case of an isotropically polarizable molecule, however it has been shown that the same form of

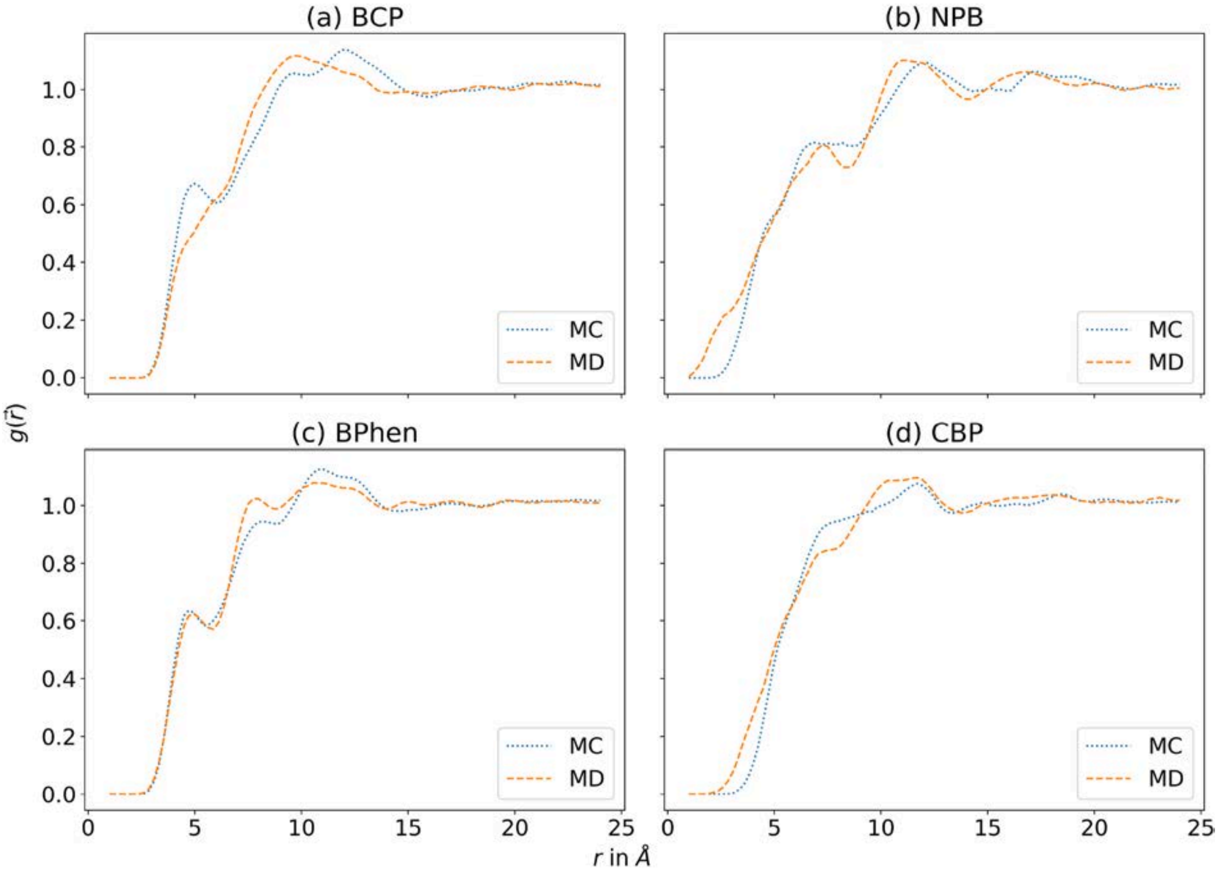

Fig. 5. Radial distribution functions for BCP (a), BPhen (b), CBP(c) and NPB (d). Dotted lines correspond to structures generated by the MC protocol, dashed lines to the MD approach.

equation can be used for the ordinary and extraordinary part under the condition that the polarizability α is not taken from a single molecule but a spherical cutout of the material, which "is sufficiently large, so that the material contained in it may be considered from a macroscopic point of view" [31]:

$$\frac{\varepsilon_u \quad 1}{\varepsilon_u \quad 2} \quad \frac{\alpha_u}{a^3} \tag{5}$$

Here u denotes the principal axis of the polarizability and a is the radius of the sphere. Notice that **equation (5)** is in the cgs unit system.

The number of atoms inside this spherical region quickly grows to several thousands, making the calculation of the dynamic polarizability computationally unfeasible, with methods like DFT. We therefor use a Thole approach with the IM-SQRT model and parameters derived by Ref. [32] to calculate the polarizability of a sphere with 3 nm radius taken from our simulated films. We then define the ordinary polarizability as $\alpha_o \quad \frac{\alpha_{xx}+\alpha_{yy}}{2}$ and the extra-ordinary polarizability as $\alpha_{\mathrm{eo}} \quad \alpha_{zz}$. The final refractive indices are given by the square root of the relative permittivities, calculated by equation (5). To exclude the influence of the different simulated densities on the absolute values of the refractive index, we correct the volume a^3 with the factor $\frac{\rho_{exp}}{\rho_{sim}}$. The final results for the ordinary and extra-ordinary refractive indices are shown in Table 1, where every value is a mean value over the 10 independent simulation runs per material and method with a statistical uncertainty of 0.01. The lower absolute values in the simulation compared to the experiment, can most likely be contributed to the inaccuracy of using the Thole model, which already underestimates the polarizability compared to DFT calculations for a single molecule (see SI). Because of this we rather compare the difference Δn between ordinary and extra-ordinary refractive index, which is a better measure for the anisotropy of the generated structure. In the MD approach only a slight anisotropy of $\Delta n \quad 0.02$ is observed for BCP, BPhen and NPB, while a bigger anisotropy of $\Delta n \quad 0.06$ is observed for CBP. Compared to experiment, Δn is strongly overestimated for all films generated by the MC approach.

Primarily the anisotropy of the refractive index should stem from an anisotropy of the orientation of the molecules in the film. To this end we have computed the orientations of the molecular fragments with respect to the normal of the film. For NPB (bottom part of Fig. 6) we find reasonable agreement between the orientation in MD and MC, but the anisotropy of the refractive index differs by a factor of three. On the other hand, for BCP, we observe a massive difference between the orientations of the core fragment (but not for the outer phenyl rings, see SI), which results an Δn which is five times as high. This indicates that the method to calculate the refractive index is very sensitive to small differences of the molecular orientations but saturates quickly at higher anisotropies.

The non-zero anisotropy for BCP, BPhen and NPB compared to the experimental data could be explained by two factors: 1. Due to the short simulation time per deposition cycle in MD, the molecules might be buried by other molecules before reaching a perfect isotropic orientation. 2. The real anisotropy might be too small to resolve experimentally (for example in Ref. [25] no material has a measured $\Delta n < 0.03$), because the experimental value is the result of a complex fit. Overall the trend of the MD structures fits the experimentally observed behaviour better, than the results obtained by the MC structures. When comparing to the fragment orientations, one can clearly see a correlation between an preferred orientation of the core fragments and the anisotropy of the refractive index.

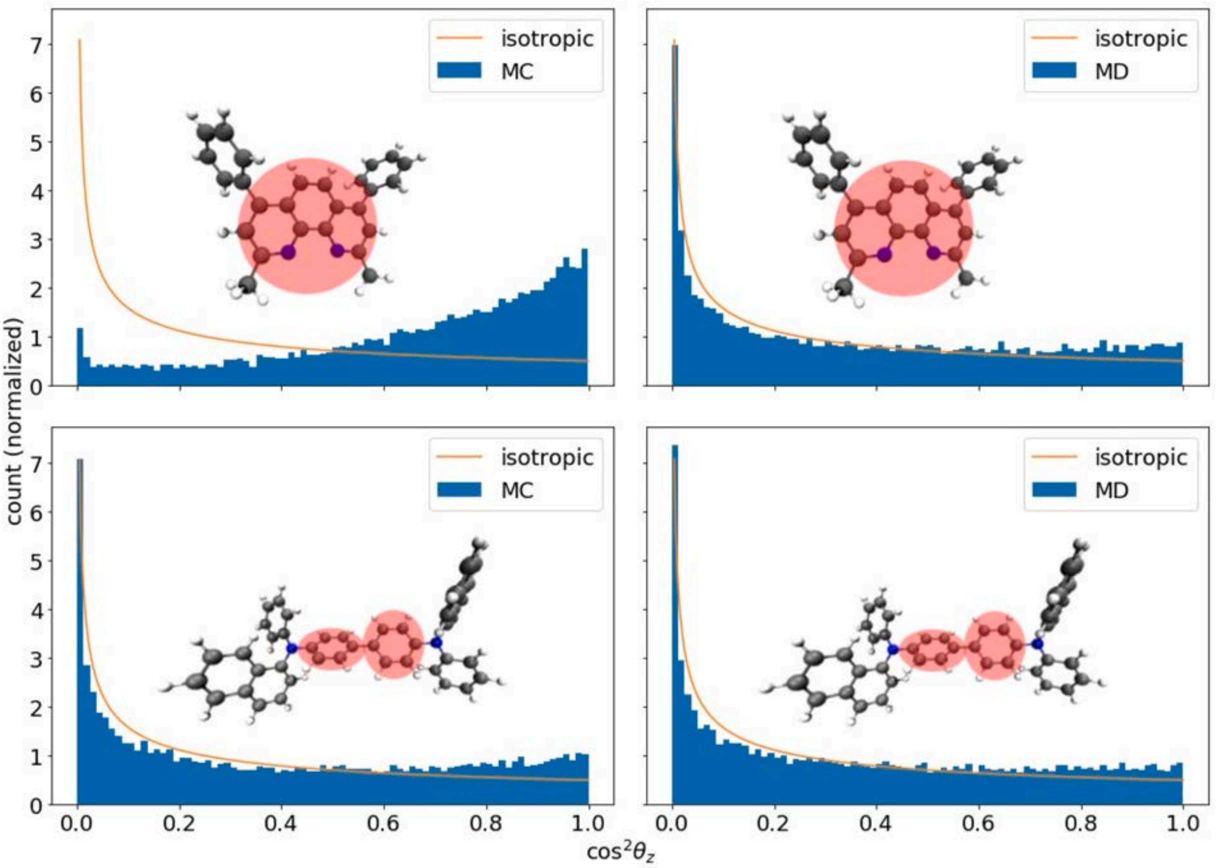

Fig. 6. Histogram for the orientation parameter $\cos^2 \theta_z$, where θ_z is defined as the angle between the normal vector of the fragment plane and the z-axis. Top: phenanthroline core of BCP, bottom: center phenyl rings of NPB. The fragment is highlighted in red, similar figures for the other dihedral fragments as well as the corresponding figures for BPhen and CBP are in the SI. The isotropic distribution is given by. (For interpretation of the references to colour in this figure legend, the reader is referred to the Web version of this article.)

Table 1
Ordinary n_o and extra-ordinary n_eo refractive index at 550 nm and their difference $\Delta n = n_\mathrm{o}$ n_eo for both simulation approaches as well as experimental values obtained by ellipsometry measurements [25].

Molecule		MC			MD		Experiment		
	n_o	neo	Δn	n_o	neo	Δn	n_o	neo	Δn
BCP	1.66	1.56	0.10	1.62	1.60	0.02	1.71	1.71	0.00
NPB	1.70	1.64	0.06	1.68	1.66	0.02	1.87	1.87	0.00
BPhen	1.72	1.60	0.12	1.68	1.66	0.02	1.73	1.73	0.00
CBP	1.72	1.58	0.14	1.68	1.62	0.06	1.80	1.74	0.06

3.5. *Charge transport properties*

Next we want to investigate how the observed morphological differences influence change transport simulations using an established workflow [33]. First we use the QuantumPatch (QP) method [34] to calculate the energy disorder σ and electronic couplings J, two factors determining transport properties in bulk OSC. σ is a measure for the width of HOMO and LUMO energy distributions, which we calculate from the $\Delta E_{\mathrm{HOMO/LUMO}}$ of 200 core molecules in the center of the film in the polarization environment of their neighbors with the QP approach using the B3LYP functional and a def2-SVP basis. For the electronic couplings, we calculate the hopping-matrix elements for dimers of charged-uncharged-pairs of 150 core molecules and their neighbors with an atom-atom-cutoff of 7 Å following the Lowdin orthogonalization procedure [35] using the BP86 functional and a def2-SVP basis. Reorganization energies λ_i are calculated based on Nelsen's four point procedure [36] for 11 arbitrary molecules in their unique environment. The geometry of charged and uncharged molecules is optimized with constraints by surrounding molecules imposed by effective core potentials (ECP) at the position of neighboring atoms.

Changes in reorganization energy are small in different deposition schemes compared to changes in disorder, therefore identical λ_i are used for both simulations of each material. The values for λ_i were: The results of the QP calculations can be found in Table 2, each σ value is the mean value of five independent samples.

We then simulated charge transport in these structures with the kinetic Monte-Carlo (kMC) charge transport protocol lightforge [37]. The atomistic morphologies and electronic properties are stochastically expanded into 40 nm × 40 nm × 40 nm structures [37] with periodic boundary conditions in x-, y- and z-direction. 20 charge carriers are initially placed into the system, resulting in a charge density of approx. 3.125×10^{-3} per site. Charge carrier movement is modelled using the Marcus rate [38].

Table 2

Results of the mobility calculations: intrinsic disorder σ_i, total disorder σ and intermolecular hopping-matrix elements $< J^2r^2 >$. For the electron transport materials BPhen and BCP all values correspond to the LUMO levels, for the hole transport materials NPB and CBP to the HOMO levels.

Molecule	MC			MD		
	σ_i [meV]	σ [meV]	$< J^2r^2 >$ [eV^2 Å^2]	σ_i [meV]	σ [meV]	$< J^2r^2 >$ [eV^2 Å^2]
BCP	40.2 ± 2.4	115 ± 5.0	2.16e-03	45.5 ± 2.0	97 ± 5.4	2.41e-03
NPB	79.6 ± 3.7	108 ± 5.4	2.09e-03	74.9 ± 4.7	110 ± 6.0	4.48e-03
BPhen	30.1 ± 1.9	122 ± 8.2	2.76e-03	42.6 ± 2.5	108 ± 7.0	3.60e-03
CBP	15.1 ± 0.6	90 ± 2.8	5.74e-03	26.7 ± 2.3	88 ± 6.4	6.42e-03

$$k_{if} \quad \frac{2\pi}{\hbar}\left|J_{if}\right|^2\frac{1}{\sqrt{4\pi\lambda k_B T}}e^{\quad\frac{\left(\lambda+\Delta E_{if}\right)^2}{4\lambda k_B T}} \tag{6}$$

with λ and J_{if} the reorganization energy and transfer integrals computed above, T the temperature (300 K) and ΔE_{if} the energy difference between this charge occupying site i and site f due to the energy disorder of the amorphous system, the applied field and the dynamic electrostatic potential of all other charges in the system. Coulomb interactions are treated explicitly with the nearest periodic copy of all other charge carriers in the system. To account for stochastics in morphology expansion and site-energy distribution, we sample and average over 10 disorder configurations per applied field. Convergence is reached if the current density is constant over two thirds of the simulation. The charge carrier mobility is calculated from the average drift-velocity of each charge carrier and applied field F as $\mu \quad \frac{v}{F}$. The resulting field dependent mobilities are plotted in Fig. 7. For BCP and BPhen the electron mobilities were calculating based on the LUMO values from Table 2, and for CBP and NPB the hole mobilities based on the HOMO values respectively. First, we observe the correct order-of-magnitude of the mobility data for all materials except BPhen on the basis of the MC morphologies [39,40,41,42]. The mobility of organic semiconductors scales as

$$\mu \sim \exp(\quad C(\beta\sigma)^{2)}. \tag{7}$$

Where β is the inverse temperature and σ is the width of the disorder distribution [43,44,45]. We note that functional dependence on σ is extremely strong. Also in eq. (6) the Marcus rate scales exponentially with the square of the site energy difference and only quadratically with the electronic coupling J. We see from Table 2 2 that the mean value of the hopping-matrix elements $< J^2r^2 >$ (where r is the distance between two pairs, see Ref. [46]) varies not significantly between the MC and MD morphologies, which is expected on the basis of the distribution functions. σ is around 100 meV for all materials, with the highest predicted valued occurring with 122 meV for BPhen and the MC morphology. This deviation is the reason why the method predicts a mobility that is too low. Also for the MD morphologies, the mobility results are in good agreement with experiment with the exception of BCP. For NPB the σ of the MD structures is slightly higher than for the MC structures which is outweighed by the much higher hopping matrix elements, resulting in an nearly identical mobility curve. For CBP the σ value is slightly lower for the MD structures, which combined with the higher hopping-matrix elements, results in a higher mobility.

To good approximation, the total disorder is given by

$$\sigma^2 \quad \sigma_i^2 + \sigma_p^2 \tag{8}$$

where $\sigma_i{}^2$ is the intrinsic disorder stemming from the distortion of the molecules upon deposition and $\sigma_p{}^2$ is the disorder stemming from the polarization effects. It is surprising that the latter depend on the morphology and we speculate that this is related to the relative orientation of the molecules. For BPhen, the $\sigma_i{}^2$ from MC is much smaller than that of MD, i.e. the "error" stems from the polarization part. For NPB the same is true. Therefore, we can conclude that for the mobility

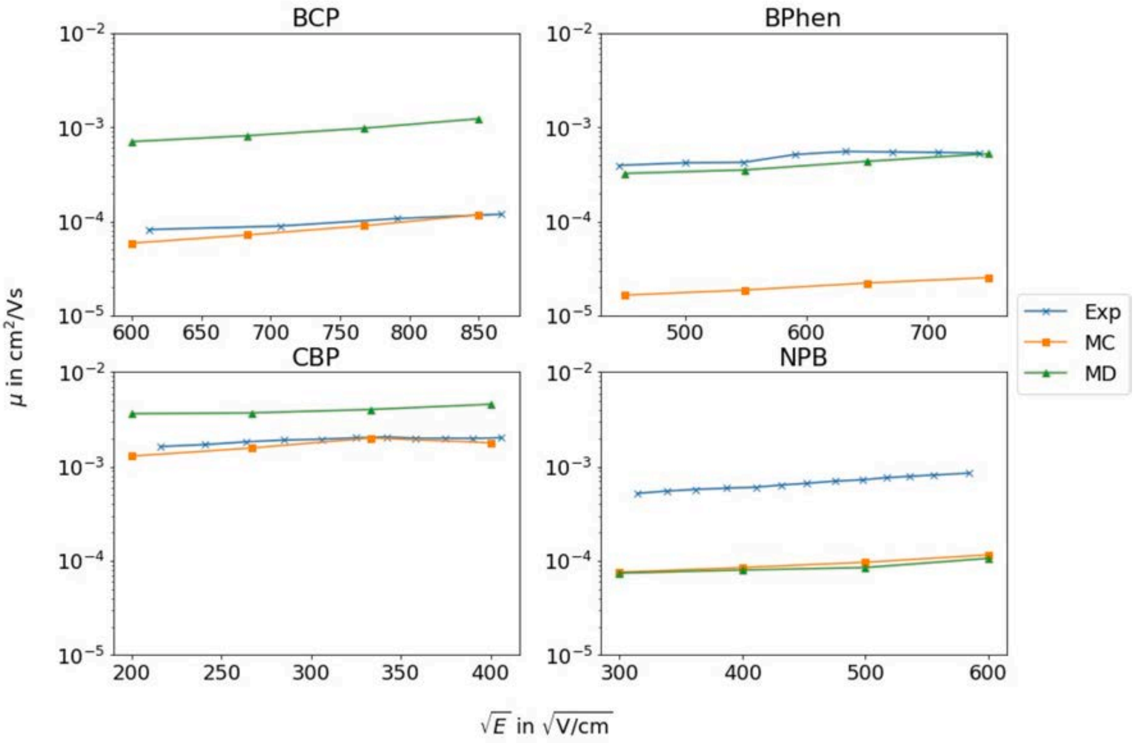

Fig. 7. Field dependent electron mobilities for BCP and BPhen and hole mobilities for CBP and NPB calculated by the KMC approach. Experimental values taken from Ref. [39] (BCP) [40], (BPhen) [41], (CBP) and [42] (NPB). Simulation errors are of the order of the symbol size.

contributions that explicitly relate to the morphology, both methods appear to generate adequate morphologies, but the more isotropic orientations of the MD films seem to induce a smaller σ_p, resulting in an overall lower mobility.

4. Conclusion

The fabrication of thin organic films via physical vapor deposition is the de facto industry standard in the production process of OLED displays. Critical device properties like outcoupling efficiency and mobility can be directly linked to the microscopic morphology. Therefore, it is important to develop accurate, yet computationally affordable procedures to model the deposition process. Collective effects may play a role at the surface of the film, but may also lead to negligible conformational changes deep in the bulk, due to the glassy nature of the material. In this work, we compared two different modeling approaches. We can show a good agreement for the density of the films generated by a molecular dynamics based approach compared to experimental results, while the films deposited with a Monte Carlo method show about 10% lower densities. To quantify the anisotropy, we calculated the ordinary and extraordinary refractive index in a Clausius-Mossotti-like approach. The difference of ordinary and extra-ordinary refractive index is overestimated in the Monte Carlo film compared to the molecular dynamics films and the experimental results. This is especially evident for BPhen and BCP where the Monte Carlo based structures show a strong anisotropy both in the calculated refractive index, as well as the orientation of their phenanthroline core, while the Molecular Dynamics based films are nearly isotropic in both cases, which is in line with experimentally available data of the refractive indices. Finally, we calculate the electron and hole mobility with our Kinetic Monte Carlo workflow and find that the fundamentally different geometric ordering of BCP and BPhen influences the electronic disorder σ and with that the final charge carrier mobility. We conclude that while the approximations made in the Monte Carlo approach can be reasonable for molecules like NPB, the full Molecular Dynamics approach is necessary to reproduce the isotropic ordering of BCP and BPhen. Overall both methods result in morphologies that can be used to predict the correct order-of-magnitude of the field dependent carrier mobility. Furthermore, we observe that the polarization part of the total disorder σ_p seems to be influenced by the orientation of molecules in the film. These results underline both the importance of (a) the prediction of the correct organic film structure on a molecular level and (b) the treatment of polarization effects for further charge transport calculations.

Declaration of competing interest

The authors declare the following financial interests/personal relationships which may be considered as potential competing interests:

Carl Degitz reports financial support was provided by Merck KGaA.

Acknowledgements

M.K. and W.W. acknowledge funding by the Deutsche Forschungsgemeinschaft (DFG, German Research Foundation) under the Research Training Group “Tailored Scale-Bridging Approaches to Computational Nanoscience” (GRK2450) and Germany’s Excellence Strategy—2082/1–390761711 (3DMM2O). We acknowledge Merck KGaA Darmstadt for fruitful discussions with respect to the morphology generation methods as well as the interpretation of the experimental data. C.D. furthermore acknowledges the funding he received from Merck KGaA Darmstadt for his PhD studies during the creation of this work. S.K. received funding by the High-Performance Computing 2 program of the Baden-Württemberg Stiftung (Project MSMEE).

References

[1] C. W. Tang, S. A. VanSlyke, Organic Electroluminescent Diodes vol. 51 (12) 913–915, publisher: American Institute of Physics. doi:10.1063/1.98799. URL https://aip.scitation.org/doi/10.1063/1.98799.

[2] H. Yersin, Highly Efficient OLEDs: Materials Based on Thermally Activated Delayed Fluorescence, John Wiley & Sons, 2019.

[3] D. Yokoyama, A. Sakaguchi, M. Suzuki, C. Adachi, Horizontal Molecular Orientation in Vacuum-Deposited Organic Amorphous Films of Hole and Electron Transport Materials 4.

[4] D. Yokoyama, C. Adachi, In situ real-time spectroscopic ellipsometry measurement for the investigation of molecular orientation in organic amorphous multilayer structures, 107 (12) 123512, http://aip.scitation.org/doi/10.1063/1.3432568. URL.

[5] S. S. Dalal, D. M. Walters, I. Lyubimov, J. J. de Pablo, M. D. Ediger, Tunable molecular orientation and elevated thermal stability of vapordeposited organic Semiconductors 112 (14) 4227–4232. doi: 10.1073/pnas. 1421042112. URL http://www.pnas.org/lookup/doi/10.1073/pnas.1421042112.

[6] D. Yokoyama, Y. Setoguchi, A. Sakaguchi, M. Suzuki, C. Adachi, Orientation control of linear-shaped molecules in vacuum-deposited organic amorphous films and its effect on carrier mobilities 20 (3) 386–391. doi: 10.1002/adfm.200901684. URL http://doi.wiley.com/10.1002/adfm.200901684.

[7] Y. Esaki, T. Komino, T. Matsushima, C. Adachi, Enhanced electrical properties and air stability of amorphous organic thin films by engineering film density 8 (23) 5891–5897. doi:10.1021/acs.jpclett.7b02808. URL https://pubs.acs.org/doi/10.1021/acs.jpclett.7b02808.

[8] M. Janghouri, E. Mohajerani, Color optimization of red OLEDs via periodic and gradient deposition rate of fluorescent dopants 51 (8) 282. doi:10.1007/s11082-019-2001-y. URL http://link.springer.com/10.1007/s11082-019-2001-y.

[9] P. Friederich, F. Symalla, V. Meded, T. Neumann, W. Wenzel, Ab Initio Treatment of Disorder Effects in Amorphous Organic Materials: toward Parameter Free Materials Simulation vol. 10 (9) 3720–3725, publisher: American Chemical Society. doi:10.1021/ct500418f. URL https://doi.org/10.1021/ct500418f.

[10] P. Friederich, A. Fediai, S. Kaiser, M. Konrad, N. Jung, W. Wenzel, Toward design of novel materials for organic electronics 31 (26) 1808256, eprint: https://onlinelibrary.wiley.com/doi/pdf/10.1002/adma.201808256. doi:10.1002/adma.201808256. URL https://onlinelibrary.wiley.com/doi/abs/10.1002/adma.201808256.

[11] T. Neumann, D. Danilov, C. Lennartz, W. Wenzel, Modeling Disordered Morphologies in Organic Semiconductors vol. 34 (31) 2716–2725. doi:10.1002/jcc.23445. URL https://onlinelibrary.wiley.com/doi/abs/10.1002/jcc.23445.

[12] H.-F. Xiang, Z.-X. Xu, V. A. L. Roy, C.-M. Che, P. T. Lai, Method for Measurement of the Density of Thin Films of Small Organic Molecules vol. 78 (3) 034104, publisher: American Institute of Physics.

[13] F. Symalla, P. Friederich, S. Kaiser, T. Strunk, T. Neumann, W. Wenzel, 26-4: computer-aided optimization of multilayer oled devices, in: SID Symposium Digest of Technical Papers, vol. 49, Wiley Online Library, 2018, pp. 340–342.

[14] F. Symalla, S. Heidrich, M. Kubillus, T. Strunk, T. Neumann, W. Wenzel, 19-4: boosting oled performance with ab-initio modeling of roll-off and quenching processes, in: SID Symposium Digest of Technical Papers, vol. 50, Wiley Online Library, 2019, pp. 259–262.

[15] F. Symalla, A. Fediai, J. Armleder, S. Kaiser, T. Strunk, T. Neumann, W. Wenzel, 43-3: ab-initio simulation of doped injection layers, in: SID Symposium Digest of Technical Papers, vol. 51, Wiley Online Library, 2020, pp. 630–633.

[16] F. Symalla, S. Heidrich, P. Friederich, T. Strunk, T. Neumann, D. Minami, D. Jeong, W. Wenzel, Multiscale simulation of photoluminescence quenching in phosphorescent oled materials, Adv. Theory Simulat. 3 (4) (2020) 1900222.

[17] N. Schmid, A.P. Eichenberger, A. Choutko, S. Riniker, M. Winger, A.E. Mark, W. F. van Gunsteren, Definition and testing of the gromos forcefield versions 54a7 and 54b7, Eur. Biophys. J. 40 (7) (2011) 843–856.

[18] W. F. Van Gunsteren, H. J. C. Berendsen, Groningen molecular simulation (GROMOS) library manual, biomos BV, nijenborgh 16, 9747.

[19] W. Huang, Z. Lin, W. F. van Gunsteren, Validation of the GROMOS 54a7 Force Field with Respect to β-peptide Folding vol. 7 (5) 1237–1243, publisher: ACS Publications.

[20] N. Metropolis, A. W. Rosenbluth, M. N. Rosenbluth, A. H. Teller, E. Teller, Equation of state calculations by fast computing machines 21 (6) 1087- 1092, publisher: American Institute of Physics. doi:10.1063/1.1699114. URL https://aip.scitation.org/doi/10.1063/1.1699114.

[21] O. M. Roscioni, G. D’Avino, L. Muccioli, C. Zannoni, Pentacene Crystal Growth on Silica and Layer-dependent Step-Edge Barrier from Atomistic Simulations vol. 9 (23) 6900–6906, publisher: American Chemical Society. doi:10.1021/acs.jpclett.8b03063. URL https://doi.org/10.1021/acs.jpclett.8b03063.

[22] L. Muccioli, G. D’Avino, C. Zannoni, Simulation of Vapor-phase Deposition and Growth of a Pentacene Thin Film on C60 (001), eprint: https://onlinelibrary.wiley.com/doi/pdf/10.1002/adma.201101652 https://onlinelibrary.wiley.com/doi/abs/10.1002/adma. 201101652. URL, vol. 23, 39, 4532-4536.

[23] S. Plimpton, Fast parallel algorithms for short-range molecular dynamics, J. Comput. Phys. 117 (1) (1995) 1–19.

[24] A.K. Malde, L. Zuo, M. Breeze, M. Stroet, D. Poger, P.C. Nair, C. Oostenbrink, A. E. Mark, An automated force field topology builder (atb) and repository: version 1.0, J. Chem. Theor. Comput. 7 (12) (2011) 4026–4037.

[25] A. Salehi, Y. Chen, X. Fu, C. Peng, F. So, Manipulating refractive index in organic light-emitting diodes, ACS Appl. Mater. Interfaces 10 (11) (2018) 9595–9601.

[26] E. Ito, Y. Washizu, N. Hayashi, H. Ishii, N. Matsuie, K. Tsuboi, Y. Ouchi, Y. Harima, K. Yamashita, K. Seki, Spontaneous buildup of giant surface potential by vacuum

deposition of alq3 and its removal by visible light irradiation 92 (12) 7306-7310, publisher: American Institute of Physics. doi:10.1063/1.1518759. URL https://aip.scitation.org/doi/abs/10.1063/1.1518759.

[27] P. Friederich, V. Rodin, F. von Wrochem, W. Wenzel, Built-in Potentials Induced by Molecular Order in Amorphous Organic Thin Films vol. 10 (2) 1881– 1887. doi: 10.1021/acsami.7b11762.

[28] T.D. Schmidt, T. Lampe, , D. Sylvinson M. R., P.I. Djurovich, M.E. Thompson, W. Brütting, Emitter Orientation as a Key Parameter in Organic Light-Emitting Diodes, 10.1103/PhysRevApplied. 8.037001. URL, https://link.aps.org/doi/10.1103/PhysRevApplied.8.037001. vol. 83.

[29] P. Friederich, R. Coehoorn, W. Wenzel, Molecular Origin of the Anisotropic Dye Orientation in Emissive Layers of Organic Light Emitting Diodes vol. 29 (21) 9528–9535. doi:10.1021/acs.chemmater.7b03742. URL https://doi.org/10.1021/acs.chemmater.7b03742.

[30] A. Salehi, X. Fu, D. Shin, F. So, Recent Advances in OLED Optical Design, URL, https://onlinelibrary.wiley.com/doi/abs/10.1002/adfm. 201808803. vol. 29, 15-1808803.

[31] K. Urano, M. Inoue, Clausius–mossotti formula for anisotropic dielectrics, J. Chem. Phys. 66 (2) (1977) 791–794.

[32] L. Jensen, , P.-O. ˚Astrand, A. Osted, J. Kongsted, K.V. Mikkelsen, Polarizability of molecular clusters as calculated by a dipole interaction model, J. Chem. Phys. 116 (10) (2002) 4001–4010.

[33] S. Kaiser, T. Neumann, F. Symalla, T. Schloder, A. Fediai, P.W. Friederich, Wenzel, De novo calculation of the charge carrier mobility in amorphous small molecule organic semiconductors, Front. Chem. 9 (2021).

[34] P. Friederich, F. Symalla, V. Meded, T. Neumann, W. Wenzel, Ab initio treatment of disorder effects in amorphous organic materials: toward parameter free materials simulation, J. Chem. Theor. Comput. 10 (9) (2014) 3720–3725.

[35] P.-O. Lowdin, On the non-orthogonality problem connected with the use of atomic wave functions in the theory of molecules and crystals, J. Chem. Phys. 18 (3) (1950) 365–375.

[36] S.F. Nelsen, S.C. Blackstock, Y. Kim, Estimation of inner shell marcus terms for amino nitrogen compounds by molecular orbital calculations, J. Am. Chem. Soc. 109 (3) (1987) 677–682.

[37] F. Symalla, P. Friederich, A. Massé, V. Meded, R. Coehoorn, P. Bobbert, W. Wenzel, Charge transport by superexchange in molecular host-guest systems, Phys. Rev. Lett. 117 (27) (2016) 276803.

[38] R.A. Marcus, On the theory of oxidation-reduction reactions involving electron transfer. i, J. Chem. Phys. 24 (5) (1956) 966–978.

[39] S.-W. Liu, C.-C. Lee, C.-F. Lin, J.-C. Huang, C.-T. Chen, J.-H. Lee, 4hydroxy-8-methyl-1, 5-naphthyridine aluminium chelate: a morphologically stable and efficient exciton-blocking material for organic photovoltaics with prolonged lifetime, J. Mater. Chem. 20 (36) (2010) 7800–7806.

[40] S. Naka, H. Okada, H. Onnagawa, T. Tsutsui, High electron mobility in bathophenanthroline, Appl. Phys. Lett. 76 (2) (2000) 197–199.

[41] H.-I. Baek, C. Lee, B.D. Chin, Comparison of the carrier mobility, unipolar conduction, and light emitting characteristics of phosphorescent host– dopant system, Synth. Met. 162 (24) (2012) 2355–2360.

[42] S. Naka, H. Okada, H. Onnagawa, Y. Yamaguchi, T. Tsutsui, Carrier transport properties of organic materials for el device operation, Synth. Met. 111 (2000) 331–333.

[43] H. Bassler, Charge transport in disordered organic photoconductors. a Monte Carlo simulation study, Phys. Status Solidi B 175 (1).

[44] H. Bassler, Localized states and electronic transport in single component organic solids with diagonal disorder, Phys. Status Solidi 107 (1) (1981) 9–54.

[45] A. Massé, P. Friederich, F. Symalla, F. Liu, R. Nitsche, R. Coehoorn, W. Wenzel, P. A. Bobbert, Ab initio charge-carrier mobility model for amorphous molecular semiconductors, Phys. Rev. B 93 (19) (2016) 195209.

[46] V. Rodin, F. Symalla, V. Meded, P. Friederich, D. Danilov, A. Poschlad, G. Nelles, F. von Wrochem, W. Wenzel, Generalized effective-medium model for the carrier mobility in amorphous organic semiconductors, Phys. Rev. B 91 (15) (2015) 155203.

Degitz, C.; Konrad, M.; Kaiser, S.; Wenzel, W.
Simulating the growth of amorphous organic thin films
2022. Organic Electronics
doi:10.5445/IR/1000143882

Degitz, C.; Konrad, M.; Kaiser, S.; Wenzel, W.
Simulating the growth of amorphous organic thin films
2022. Organic Electronics, 102, 106439.
doi:10.1016/j.orgel.2022.106439